The physics of nanowire superconducting single-photon detectors

Renema, J.J.

Chapter 4

Experimental Test of the Detection Models in Nanowire Superconducting Single-Photon Detectors

We report an experimental test of the photodetection mechanism in a nanowire Superconducting Single-Photon Detector (SSPD). Detector tomography allows us to explore the 0.8-8 eV energy range via multiphoton excitations. High accuracy results enable detailed comparison of the experimental data with theories for the mechanism of photon detection. We show that the temperature dependence of the efficiency of the SSPD is determined not by the critical current but by the current associated with vortex unbinding. We find that both quasiparticle diffusion and vortices play a role in the detection event[1].

4.1 Introduction

Superconducting nanowire single-photon detectors (SSPDs or SNSPDs) [1, 2] are currently the most promising detection systems in the infrared, achieving detection efficiencies of up to 93% at 1550 nm [55]. Despite these technological advances, the fundamentals of the working principle of these detectors are poorly understood and under active investigation, both theoretically [18, 24, 25, 33, 70, 71, 73, 74] and experimentally [8, 16, 15, 23, 56, 75, 76, 77, 78, 79, 80, 81].

[1] This chapter is based on J.J. Renema *et al.* Phys. Rev. Lett., **112** (11), 117604 (2014).

A typical SSPD consists of a film of a superconducting material such as NbN or WSi, a few nm thin, nanofabricated into a meandering wire geometry. When biased sufficiently close to the critical current of the superconductor, the energy of one or several photons can be enough to trigger a local transition to the resistive state, resulting in a detection event. The energy of the absorbed photon is distributed through an avalanche-like process, creating a nonequlibrium population of quasiparticles. This quasiparticle population then disrupts the supercurrent flow, resulting eventually in a detection event.

In this chapter, we adress the nature of this disruption, which lies at the heart of the photodetection mechanism in SSPDs. At present, there are three important open questions. First: it is unknown whether the detection event occurs when the energy of the incident photon causes a cylindrical volume inside the wire to transition to the normal state (see Figure 4.1a) [1], or whether it is enough for the superconductivity to be weakened but not destroyed by the depletion of Cooper pairs over a more extended region (see Figure 4.1b) [18].

The second open question is whether magnetic vortices play any role in the detection mechanism. There are two varieties of vortex-based models. The first is an extension of the normal-core model, in which a vortex-antivortex pair forms at the point where the photon is absorbed (Figure 4.1c) [33]. In the second, the weakening of superconductivity lowers the energy barrier for either a vortex crossing [24, 82] or a vortex-antivortex pair crossing (Figure 4.1d).

The last open question pertains to the temperature dependence of the photoresponse of SSPDs. Intuitively, one would expect the SSPD to be less efficient at lower temperatures, as the detector works by breaking superconductivity and the energy gap of a superconductor decreases with increasing temperature. However, the opposite effect is consistently observed [8]. Apart from a study of the temperature dependence of the diffusion constant [73], no real headway has been made in this problem.

Our experimental results provide answers to all three questions. In short, we show that both quasiparticle diffusion and vortices play a role in the detection event. We achieve the first result by measuring the functional dependence between the bias current and the photon energy required for a constant detection probability. The observed linear functional dependence is incompatible with the original hotspot model and demonstrates the importance of diffusion. Our evidence for the role of vortices lies in the observation of a reference current which sets the efficiency of the detection mechanism and which is unequal to the critical current and also has a different temperature dependence. At the temperature where the reference current crosses the critical current, the efficiency of the detector degrades. We find that the temperature dependence of the reference current matches that of the current at which vortices can unbind from the sides of the detector.

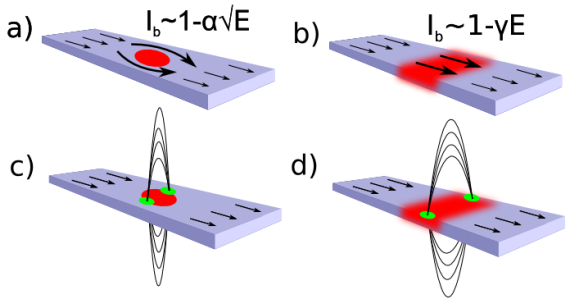

Figure 4.1: Sketches of the four main detection models. *a)* In the normal core-hotspot model, the photon energy creates a normal domain inside the superconductor, which the current has to bypass. *b)* In the diffusion-based hotspot model, the quasiparticles diffuse outward from the point of absorption, creating a band of depleted superconductivity. *c)* In the vortex nucleation model, a vortex-antivortex pair is formed in the hotspot. *d)* In the vortex crossing model, either a vortex or a vortex-antivortex pair *(pictured)* uses an area of weakened superconductivity to cross the wire and annihilate. Picture is not to scale.

4.2 Experiment

We perform the majority of our experiments on a 220 nm wide bow-tie nanodetector [39]. The detector is patterned from a 5 nm thick NbN film deposited on a GaAs substrate. The detector is fabricated by electron beam lithography and reactive ion etching. Photodetection takes place in the narrow (w_0 = 220 nm wide) part of the bow tie, where the current density is highest.

Compared to Chapter 3 and previous experiments [8, 16], we significantly extend the energy range over which we probe the detector. The energy range in our experiment runs from 0.75 eV to 8.26 eV, corresponding to λ_{eff} = 1650 nm - 130 nm, whereas the energy range in Chapter 3 ran from 1500 nm - 325 nm. We achieve this extension of the energy range by using multiphoton excitations, which are resolved by detector tomography [36, 49, 67, 83]. Detector tomography is a method of quantum detector characterization that relies on illuminating a photon detector with a series of known quantum states and observing the photoresponse. In our case, we use coherent states from a broadband supercontinuum laser, which is spectrally filtered[2]. These states have known photon number distributions which are set by the classical laser intensity, which can be easily varied. From this, we determine the response to each individual number of photons, i.e. the Fock-

[2]More details may be found in the Appendix to this chapter.

basis response[3]. The strength of our modified detector tomography is that it allows us to separate the incoupling and absorption efficiency η, i.e. the probability to absorb a photon, from the internal detection probability p_n, i.e. the probability of a detection event given the absorption of n photons. A detailed description of our method can be found in Chapter 2, and in the Appendix to this chapter.

4.3 Results and Discussion

Figure 4.2 shows the measured combinations of bias current I_b and photon energy $E = n(hc/\lambda)$ for which the detection probability equals 1% after absorption of n photons. We achieve this result by performing detector tomography at twelve different wavelengths, and finding the current at which n photons (indicated in the legend) have the required probability to cause a detection event.

To validate our experimental method of using multiphoton excitations to probe the detection mechanism, we measured at wavelengths that are harmonics (e.g. $\lambda = 1500$ nm and $\lambda = 500$ nm). We consistently find that the results of these measurements overlap over the entire measurement range, and have indicated these points with arrows in Figure 4.2. This demonstrates that, irrespective of which detection model is correct, the observed probabilities p_n depend only on bias current and overall excitation energy $E = n(hc/\lambda)$. This is an independent justification of the use of multiphoton excitations to test the detection mechanism.

We can parametrize our complete set of measurements by the expression $I = I_0 - \gamma E$, where I is the observed current required to achieve $p_n = 0.01$, and E is the overall energy of the excitation. The slope γ describes the interchange between bias current and photon energy. By extrapolating to E = 0, we find a current I_0 that is unequal to the critical current I_c and which we name the *reference current*, since it functions as the baseline from which the detector response may be determined. At $T = 3.2$ K, we find $I_0/I_c = 0.75$. This experimental result does not change significantly with the choice of threshold criterion. The linear relation persists; a 10% threshold criterion[4] gives $I_0/I_c = 0.79$.

In the regime $I_0 < I_b < I_c$, all multiphoton detection probabilities p_n of the detector are constant. However, we find that the linear efficiency η increases in this regime. We attribute this to the fact that in our bow-tie structure, a larger area of the detector is above I_0. It is known that for efficient meander detectors, there is a plateau region where the detector response is constant with current [55]. We note that dark counts occur in

[3] See Chapter 2 for extensive discussion

[4] With the results presented in Chapter 5, we will be able to investigate in Appendix II of that chapter what the precise consequences are of choosing a threshold criterion $p_n \ll 1$ on the observed energy-current relation.

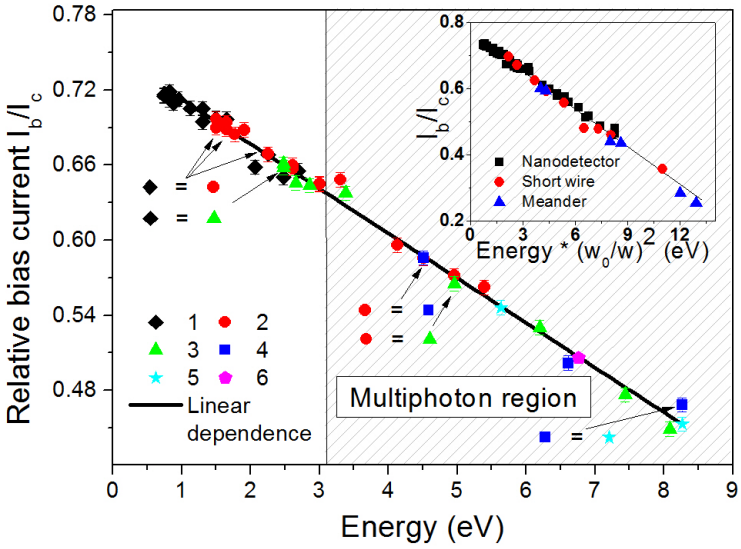

Figure 4.2: Quantum tomography of superconducing single-photon detectors. We plot the bias current required to obtain a 1% probability of a given detection event, as a function of the overall energy of the multiphoton excitation. The points are the experimental data; their shape and colour indicate the number of photons associated with each excitation. The arrows indicate those points where two photon energies coincide. The line shows a linear interchange between bias current and excitation energy. The shaded area indicates the regime that is only accesible with multiphoton excitations. *Inset*: comparison of a nanodetector, a short (200 nm) wire, and a meander. We find that the response of the wire and meander coincides with that of the nanodetector, taking into account the difference in width between these three detectors by normalization to the width w_0 of the nanodetector.

our system when $I_b \approx I_c$. Around I_0, we do not measure any dark counts in a 30 s interval. This demonstrates - suprisingly enough - that extrapolation to $E = 0$ does not yield the dark count rate.

Figure 4.2 demonstrates that the relation between bias current and photon energy required to have a constant detection probability is linear over one order of magnitude in energy. This result demonstrates that the detection process is not associated with any normal-state region that is formed in the SSPD. For a normal-core model, the energy dependence would be quadratic, as can be seen from a simple geometric argument that relates the lateral size of the obstruction made by the normal core to the photon energy [16]. For a model in which there is no normal state, the current-carrying capacity of the wire is linearly dependent on the number of remaining Cooper pairs and therefore on the photon energy.

We will now demonstrate that we can use our nanodetector as a model system of an SSPD. We compare our results with those on a $w = 150$ nm wide, 400 nm long wire and a conventional $w = 100$ nm meander detector[5]. The inset of Figure 4.2 shows a comparison of our three detectors. We take into account the width w of the detector by normalizing the energy scale to the width of the nanodetector, which enters through both the critical current and through the intrinsic $1/w$ scaling of the detection mechanism [16]. For our nanodetector, wire, and meander, the results superimpose. This demonstrates that our nanodetector functions as a model of an SSPD.

Figure 4.3 shows the experimental observations at $\lambda = 600$ nm, for the $n = 1$ to $n = 4$ photon regime. By restricting ourselves to one wavelength, we can improve the accuracy of our experiment by removing all systematic errors associated with changing wavelength[6]. This data is representative for the accuracy of our experimental runs at other wavelengths. We fit a general expression $I = I_0 - \gamma E^{\alpha}$ to this selection. As noted above, we expect to find $\alpha = 0.5$ for the normal-core hotspot model and $\alpha = 1$ for a diffusion-type model. For the vortex-based models, the expressions are more complex, but can be approximated by $\alpha = 0.5$ for the vortex nucleation model[7], and by equation 1.6 for the vortex crossing model[8][16, 24, 25, 33].

We find experimentally $\alpha = 1.00 \pm 0.06$, indicating good agreement with the diffusion model. We note, however, that since the most straightforward variant of the diffusion model predicts $I_0 = I_c$, this cannot be the whole story. We must therefore look for additional effects to explain the detection mechanism in SSPDs.

[5] More details may be found in the Appendix to this chapter.

[6] We will see in Appendix II of this chapter that at least some of those systematic errors may be associated with crossing the GaAs bandgap at $\lambda = 816$ nm.

[7] For the vortex nucleation model, we have set $\gamma = 0$ in the terminology of [16] throughout. This is a reasonable approximation for our experimental situation.

[8] In our original article, we claimed that the vortex nucleation model can be approximated as $\alpha = 0.75$. This is incorrect. We present here both the original fit for ($\alpha = 0.75$) and the fit to equation 1.6, which is the correct function. We note that this error does not alter the conclusions of this chapter.

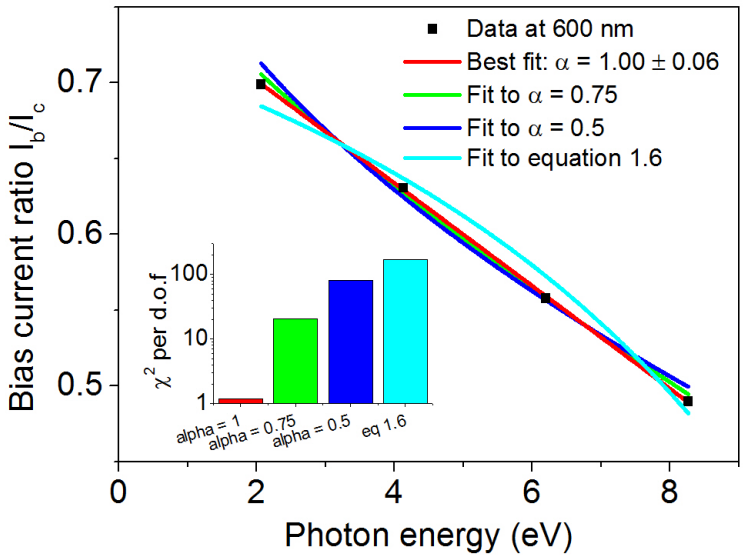

Figure 4.3: Experimental results on quantum detector tomography at $\lambda = 600$ nm. We show a single run of the experiment from Figure 4.2. To this data, which is free of the systematic error associated with changing wavelength, we fit a general expression $I = I_0 - \gamma E^{\alpha}$, where the value of α determines which model we are in. We find $\alpha = 1.00 \pm 0.06$, indicating good agreement with the linear (diffusion) model. We plot fits to $\alpha = 0.5$ and $\alpha = 0.75$ for comparison, as well as to equation 1.6. *Inset:* χ^2 of the four fits. We find that scenarios with a nonlinear energy-current relation are strongly inconsistent with our experimental data.

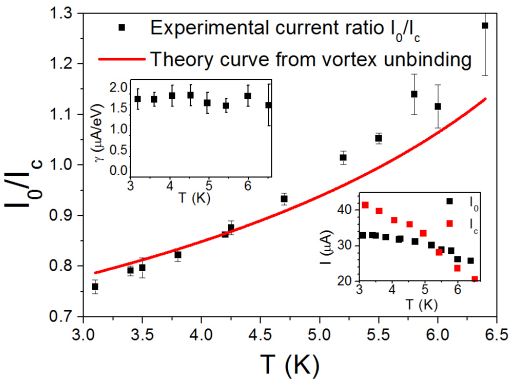

Figure 4.4: Temperature dependence of the fundamental current I_0 in the nanodetector, relative to the critical current. The red curve shows the temperature dependence of the ratio of the current associated with the vortex energy barrier (the barrier that a vortex has to overcome to enter the device), and the Ginzburg-Landau critical current [24, 25]. *Top inset*: Temperature dependence of the energy-current interchange ratio γ. This parameter, and the overall linear efficiency η are both temperature independent to within our experimental accuracy. *Bottom inset:* Temperature dependence of I_0 and I_c, separately. I_c follows the temperature dependence of the Ginzburg-Landau depairing current.

In Figure 4.4, we show the temperature dependence of the observed reference current I_0, measured on the nanodetector, normalized to the experimental critical current. We obtain this plot by performing an experiment as shown in Figure 4.2 at various temperatures. We find experimentally that only the current scale I_0 is temperature dependent; the incoupling efficiency η and energy-current slope γ are independent of temperature. The temperature dependence of I_0 therefore completely describes the temperature behaviour of the device. I_c follows the Ginzburg-Landau temperature dependence, which is consistent with the result found on Nb bridges [84]. The key result from Figure 4.4 is that the temperature dependence of the reference current is different from that of the critical current.

We first discuss the implications of our results for the practical use of SSPDs. Around $T = 5.5$ K, we find $I_0 \approx I_C$. This means that above this temperature, there are energies for which the detector no longer operates fully as a single-photon detector. This observation explains the strong reduction in performance that detectors experience around this temperature. Note that with the usual semiclassical characterization, one can always find a regime where measured count rates are linear with input power by going to sufficiently low power, even at $p_1 \ll 1$. The transition from single to

multiphoton detection that we have found can therefore only be observed by the use of detector tomography.

Our experimental I_c follows the Ginzburg-Landau $I_c(T) = I_c(0)(1 - T/T_c)^{3/2}$ dependence of the depairing current, i.e. the current at which the Cooper pair binding energy is reduced to zero. The reference current I_0 has a different temperature dependence. As vortices are the other major effect in type-II superconductors, it is natural to consider whether the observed current scale pertains to vortices. Vortices are affected by the Lorentz force, and an unpinned vortex would be driven across the width of the strip by the bias current. We must therefore consider dynamic vortex scenarios.

Based on the above considerations, we compare the reference current to the current scale that governs the height of the energy barrier for a vortex crossing [24, 25]. The ratio I_0/I_c contains an explicit temperature dependence through the superconducting coherence length $\xi(T) \sim (1 - T/T_c)^{-0.5}$ ($T_c = 9.6$ K). In Figure 4.4, we plot this temperature dependence. The existence of an alternate current $I_0 \neq I_c$ in SSPDs, and the observation that the temperature dependence of this current follows the temperature dependence of the binding energy of a vortex is evidence for the fact that the detection mechanism is vortex-based and that the temperature dependence is set by this energy.

SSPDs can also be used in the keV regime, either for detecting X-ray photons [85] or for detecting ions. The experiment by Suzuki *et al.* [75] on ion detection in 800 nm wide, 10 nm thick detectors has clearly demonstrated that the normal-core hotspot model is correct in the keV range. This is understandable, as a single injection of a large amount of energy will be enough to break all the Cooper pairs at a single position along the wire, leading to a normal-core scenario. There must therefore be a typical energy where the diffusion-based scenario gives way to a normal-core scenario. By fitting only low-energy events and extrapolation to high energies, we can check whether all our results are described by a single model. We find that this is the case, and therefore conclude that this transition occurs at an energy higher than 8 eV, for our system.

The overall conclusions which may be drawn from our results are that both vortices and diffusion play a role in the detection event. Returning to Figure 4.1, we may therefore conclude that scenario d) is the one that corresponds closest to reality. We note, however, that the particular vortex crossing model proposed by Bulaevskii *et al.* has a energy-current dependence that does not correspond to our experimental observations. This point was adressed in a recent article by Engel *et al.* [28], which combines diffusion and vortex crossing in a numerical simulation. However, both the numerical simulation and the theoretical work predict $I_0 = I_c$ for the limit $T \to 0$. More theoretical work is needed to explain our results.

4.4 Conclusion

We have demonstrated experimentally that the dependence between the excitation energy and bias current required to produce a detection event in a superconducting single-photon detector is linear. The exact linear dependence in the experiment is consistent with a detection model that relies on the diffusion of quasiparticles produced by the initial excitation. Other models produce behaviour that deviates significantly from linear dependence.

We find a current scale which characterizes the response of the detector which is unequal to the critical current of the device. When the temperature is increased, we find that the observed current scale exceeds the critical current at the same temperature where the SSPD response degrades. We observe no temperature dependence in the other observed parameters, which together provide a complete description of the detector. We therefore conclude that we have localized the problem of temperature dependence of SSPDs to a single current scale. The observed temperature dependence matches reasonably well with a theory describing the crossing of a single vortex. From our results, it is clear that at optical frequencies, quasiparticle diffusion and vortex unbinding are the two main ingredients in any model of SSPD behaviour.

4.i Appendix: Supplementary Material[9]

4.i.1 Detector Tomography

Detector tomography provides the probability of a detection event without relying on any assumptions about the detector. We therefore do not need to consider the inner workings of each model, but treat them agnostically, i.e. no assumptions about the properties of the detector or the parameters of the models go into our experimental results. This is particularly necessary in the present situation, where there is no consensus on which physics is relevant for the photodetection process.

Our method relies on observing nonlinearities in the detection probability of the device as a function of input power. For this reason, we are completely insensitive to the amount of overlap between the light beam and the active area of the detector [67]. This is a requirement, because our detector is subwavelength, and therefore the spatial overlap between our detector and the input mode is necessarily small. Detector tomography enables us to simultaneously measure the fraction of detection events caused by each multiphoton process. We model the detection efficiency by:

$$R_{click} = 1 - e^{-\eta N} \sum_{n=0}^{n_{max}} (1 - p_n) \frac{(\eta N)^n}{n!}, \tag{4.1}$$

where R_{click} is the observed detection rate and N is the mean photon number of the incident coherent state. n_{max} is the photon regime which the detector is operating in, which is determined by model selection (see below). η is the linear efficiency (which is discarded in further analysis) and the p_n are the quantities of interest: they represent the probability of a detection event, given that n photons are absorbed in the detector.

4.i.2 Determination of the Photon Regime

The parameter n_{max} in equation 4.1 sets the maximum number of photons that is still participating in the detection process in some nontrivial way, i.e. which photon regime the detector is in. We determine n_{max} by making a series of fits to each n (up to $n = 6$) and computing the goodness-of-fit statistic χ^2 per degree of freedom. For a good fit, we should find $\chi^2 \approx 1$. First, we reject all fits with $\chi^2 \gg 1$. Then, we pick the fit that has minimal χ^2. Based on model selection theory, we should use the Akaike Information Criterion AIC $= \chi^2 + 2n_{max}$ to pick the model which describes the data with fewest parameters [86]. In practice, we find that well-fitting models all have the same χ^2 and badly fitting models produce much larger χ^2 . Therefore,

[9] This section is based on the Supplementary Material to J.J. Renema *et al.*, Phys. Rev. Lett., **112** (11), 117604 (2014).

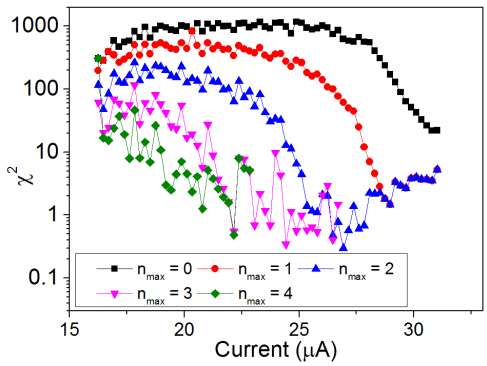

Figure 4.5: Goodness-of-fit parameter χ^2 as a function of bias current. This experiment was performed on the nanodetector. $\chi^2 \approx 1$ indicates a good fit. Each line corresponds to a model where the detector is in a particular multiphoton regime. From this graph, we determine the multiphoton regime which the detector is in. To find the appropriate photon regime, we select the curve with minimal χ^2 that has the lowest n_{max}.

minimizing the AIC is equivalent to finding the first model with a low χ^2, which is the procedure that we described in Chapter 2.

Figure 4.5 shows a typical result (in this case for a measurement at $\lambda =$ 600 nm) of χ^2 for the various models as a function of bias current. The top curve (black squares) shows the detector modelled as a one-photon detector, i.e. $p_i = 1$ for $i \geq 1$ (i.e. $n_{max} = 0$). For currents above 28.5 μA, the detector can be described by a model with $p_i = 1$ for $i \geq 2$ (i.e. $n_{max} = 1$). When we decrease the current below 28.5 μA, the detector is well described by a model with $p_i = 1$ for $i \geq 3$ (i.e. $n_{max} = 2$), and so on.

4.i.3 Experiment

The detectors were illuminated with a Fianium broadband laser, with a specified pulse duration of 7 ps and a repetition rate of 20 MHz. In the present experiment, we used optical wavelengths from 460 nm to 1650 nm. For each experimental run, we selected a band of $\Delta\lambda = 10$ nm via dichroic mirrors, high and low edgepass filtering and bandpass filtering with a dielectric filter.

It was reported that operating the detector at high count rates compared to its intrinsic reset time can result in a spurious nonlinear response [87]. To avoid this issue, we discard all data where the fraction of pulses that results in a detection event is higher than $e^{-2} \approx 0.14$.

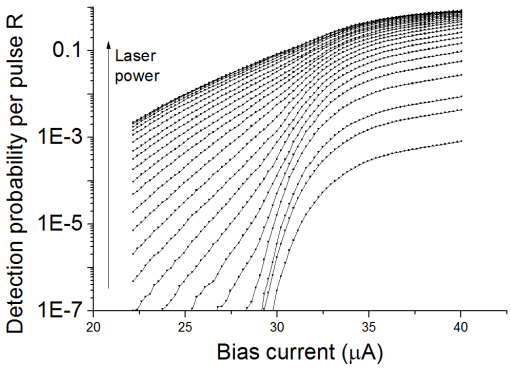

Figure 4.6: Raw experimental data for a single measurement run at 1400 nm. We plot the observed detection probability per pulse as a function of bias current, for various laser intensities. Note that the laser powers are not spaced uniformly.

4.i.4 Example

To illustrate our measurement procedure, we demonstrate our data processing on the experimental run at λ =1400 nm. In Figure 4.6, we plot our raw data. We measure the detection probability as a function of bias current at various laser powers.

This figure is best understood by reasoning outwards from the low-power graph at the bottom-right. At low powers, we measure the usual response which is also seen in SSPDs: at low currents, we find a region where the detection rate increases rapidly when the bias current is increased, whereas at high currents the response is more or less independent of bias current. For SSPDs, the flatness of this plateau is sometimes taken as an informal measure of the quality of the device. In our case, this rule of thumb is not applicable since we have an intrinsicly nonuniform geometry. We discuss this point further in a separate section of this Appendix.

When we increase the laser power, two effects occur. At low currents, we observe detection events with a superlinear dependence on power, indicating that we are in a multiphoton regime. Secondly, at high currents we observe saturation of the detector.

Figure 4.7 shows the data processing. We convert the bias-current dependent curves into power-dependent curves. The arrow indicates the direction of increasing bias current. We fit equation 4.1 to these curves, and then apply model selection as described above. We consistently find that we are able to fit our entire data set with equation 4.1, obtaining values for η, and p_i for each bias current.

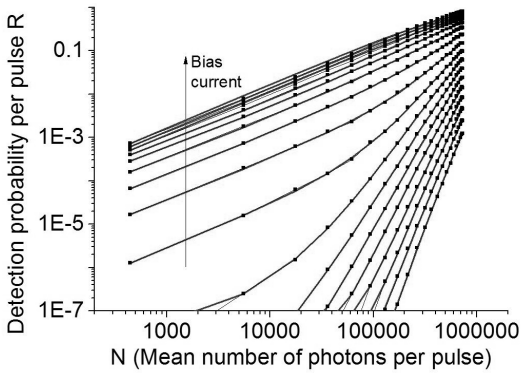

Figure 4.7: Experimental data as a function of mean photon number per pulse. The black points show the experimental data from figure 4.6, but plotted as a function of photon number. The black curves show fits to equation 4.1. We select the optimal fit via model selection.

In Figure 4.8, we plot the measured values of p_i as a function of bias current. Furthermore, as a comparison, we plot the scaled low-power detection probability. The fact that the low-power count rate and p_1 have very similar functional dependencies on I_b serves as a consistency check. At higher photon numbers, the relation between observed count rates and p_i is nonlinear, as can be seen from equation 4.1.

The dashed line represents the threshold criterion used for the figures in the main text. We note that the threshold criterion is far away in current from the current where our model selection switches from one model to the next. Therefore, the accuracy with which we can determine the threshold current is independent of the precise method of model selection.

4.i.5 Error Analysis

The accuracy with which we can measure p_i is crucial to our argument regarding the linearity of the energy versus bias current relation at constant p_i. We perform error analysis in three different ways. First, we obtain estimated errors from the fit to equation 4.1, which give us errors on the point $p_i = 0.01$ through standard error propagation techniques. We validate these errors in two ways. First, we perform a calculation where we split a data set where we integrated for 30 s at each measurement setting into three blocks of 10 s. We analyze these blocks separately and compare the spread in observed p_i. Secondly, we perform several subsequent experiments under exactly the same conditions, and compare the spread in p_i. From this analysis, we conclude that $\Delta I_b = 50$ nA is a reasonable estimate of our

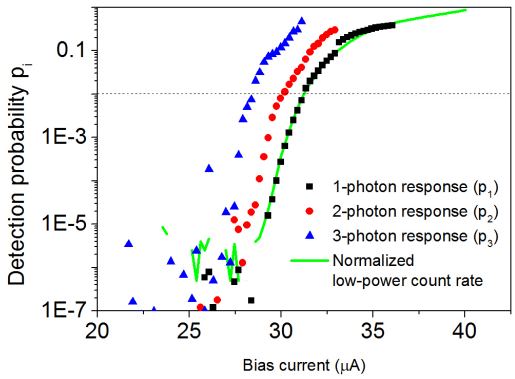

Figure 4.8: Detection probabilities for absorbed photons as a function of bias current.

error in determining the point where $p_i = 0.01$. The fact that the error on subsequent experiments is not larger than that of a series of interleaved measurements is proof that our setup is stable over the required measurement times.

4.i.6 Samples

The properties of our three samples at 3.2 K are:

	nanodetector	wire	meander
Width w (nm)	220	150	100
Thickness (nm)	5	4.7	5
Length	-	200 nm	105 μm
$I_c(\mu A)$	44	28	23
$I_0(\mu A)$	33.9	21.5	17.6
γ (μA/eV)	1.6	2.7	4.4

4.i.7 Localization of the Detection Response[10]

Since our detector is inherently inhomogeneous in width, it is necessary to consider whether photon absorption events in the areas far away from the center of our detector can be responsible for detection events. We demonstrate that this is not the case by estimating first the size of an excitation at the center of the detector, and then demonstrating that excitations which are further away than that do not cause detection events.

[10] See also Chapter 7.

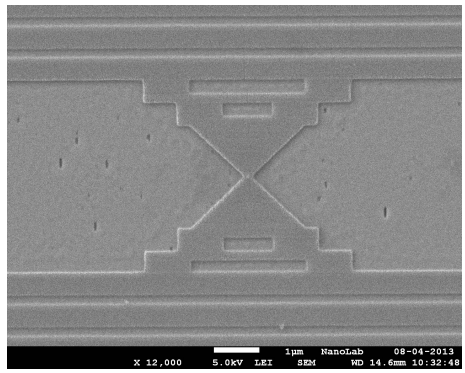

Figure 4.9: SEM image of a detector nominally identical to the one used in this experiment. The active area of this device is in the very center of this image. The white bar represents a distance of 1 μm.

First, estimates of the timescale involved in the detection process range from $\tau = 2.7$ ps [28] to $\tau = 20$ ps [40]. Combined with a diffusion coefficient of $D = 0.5$ cm^2/ s, this gives an excitation size of $x =$ 10-30 nm. We note that the lower estimate is close to the resolution with which our constriction is defined. For photons which are absorbed further away than that, the current density is much lower due to the large taper angle of 45 degrees. For example, if the detector is operated at $I_b/I_c = 0.75$ at the constriction, the current density 50 nm away from the constriction will be only $I_b/I_c = 0.5$. Moreover, the additional width of the detector at that point means that the detection probability is correspondingly lower.

From the scaling demonstrated in the inset in Figure 4.2, we can estimate that when the detector is in the 1-photon regime for 400 nm photons on the constriction, it will be in the 4-5 photon regime for photons absorbed 50 nm away from the constriction. The orders of magnitude discrepancy in count rate associated with such a difference in photon regimes means that the contribution from areas outside the narrowest part of the constriction is negligible. This demonstrates that we are justified in considering our detector as a single line-segment.

4.i.8 Temperature Dependence of λ_c

As a consistency check, we demonstrate that our work reproduces previous experimental results that were obtained without the use of tomography. In previous work [73], the temperature dependence of the SSPD was described in terms of a cutoff wavelength λ_c, in the form of an empirical formula for the detection rate $R(\lambda) = 1/(1 + (\lambda/\lambda_c)^n)$. This cutoff wavelength was observed to be both temperature and current-dependent. At high currents, the temperature dependence is stronger.

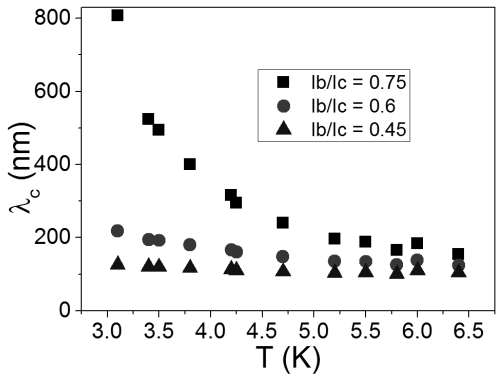

Figure 4.10: Temperature dependence of the cutoff wavelength as a function of relative bias current.

We compare our results to those of [73] by converting our energy-current dependence into a cutoff wavelength. The criterion for λ_c is equivalent to $p_i = 0.5$. We solve the equation $\alpha I_c = I_0 - \gamma E$ for $E = hc/\lambda_c$, where $\alpha = I_b/I_c$ is the bias current ratio. In Figure 4.10, we plot the result of this computation. We find that we are able to reproduce the experimental result from [73]: the observed current scale reproduces the behaviour that was observed for a TaN SSPD. In particular, at low currents, the cutoff wavelength is small (high energy) and barely dependent on temperature. At high currents and low temperatures, the cutoff wavelength increases and is in the infrared. This reproduces the earlier experimental observation that it is the IR response of the detector that is most strongly affected by elevated temperatures.

4.ii Appendix: Wavelength Measurements with an SSPD

The observation that a superconducting single-photon detector is sensitive to the overall energy of the excitation naturally gives rise to the question whether this effect can be used to measure the wavelength of an incident beam, and if so how accurately. Motivated by this question, we performed quantum detector tomography on a 150 nm wide superconducting single-photon detector in a narrow wavelength range, from $\lambda = 840$ to 900 nm, using a series $\Delta\lambda = 10$ nm FWHM filters in steps of 20 nm. We increased the integration time in our experiment to 10 s per point, which leads to increased accuracy in our measurements. Furthermore, we enhanced the count rate somewhat (from $\ll 1$ MHz to ~ 0.5 MHz) which increases the overall accuracy with which we can determine p_1.

The natural application of such a device would be as a spectrometer, as was already proposed in 2007 by Reiger *et al.* [88]. The operating principle of an SSPD-based spectrometer would be that the bias current is swept, and the counts recorded. Using the fact that the threshold current (i.e. the current at which one observes detection events) is different for each wavelength, one could in principle reconstruct the spectrum from the observed count rate dependence on bias current.

There are several good reasons to be skeptical about the practicality of such a device. First of all, it has energy resolution only in a statistical sense. Unlike a grating-based spectrometer, there is no intrinsic information gained about each photon individually, only about the whole in a statistical sense. This means first of all that the amount of signal is abysmal (the device operates by deliberately not detecting a large portion of the incident photons) and secondly that sources which are varying in time cannot be characterized. A second reason is that it is unclear how narrowly-spaced wavelengths would be separated. The spectral width $\Delta\lambda$ of our illumination in this experiment is already larger than the observed accuracy. While we will show that we can measure the central wavelength of our incident laser beam with an accuracy of a few nm, it is unclear how two adjacent wavelengths would be separated. In [88], this was done for light of $\lambda = 900$ nm and $\lambda = 530$ nm, but this resolution is far away from any practical significance.

For these reasons, we include our results on this topic in this thesis more as a demonstration of the abilities of our methods and as an exploration of the ultimate accuracy of our system than as a concrete route to any practical application. However, since SSPDs operate across a broad range of wavelengths (from X-ray to mid-IR) and are robust for space applications, we cannot exclude that there is some application, perhaps in astronomy, at some exotic wavelength where the results presented here will prove useful.

We show the result of our quantum detector tomography experiment in Figure 4.11. We report data for four wavelengths: 900 nm, 880 nm, 860 nm

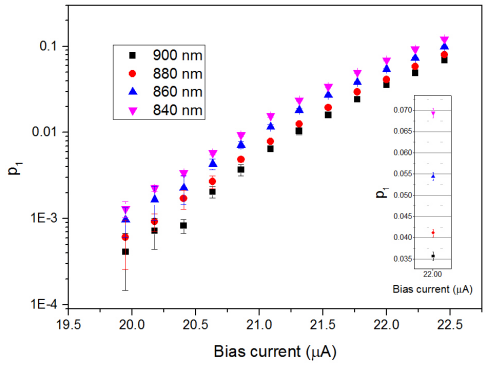

Figure 4.11: Quantum detector tomography of a superconducting single-photon detector at a series of narrowly spaced wavelengths

and 840 nm. We find the usual effects for SSPDs: lower photon energy as well as lower bias current lead to lower detection probability. In the inset of Figure 4.11, we show a zoom-in on one experimental point, demonstrating the observed values of p_1 at a bias current of 22.0 μA. The error bars in the figure correspond to the error estimate from our tomographic fits.

In Figure 4.12, we show the accuracy which is computed from the experimental data presented in Figure 4.11. We define this accuracy as $2(p_1(\lambda_1) - p_1(\lambda_2))/(\sigma_{p1(\lambda 1)} + \sigma_{p1\lambda 2})$, where σ is the error with which we determine the value of p_1 for a particular wavelength. That is: we measure how many error bars away two adjactent points are. This is a measure of how accurately we can determine the center wavelength of a particular quasi-monochromatic light source.

We find that this accuracy depends on the applied bias current. This is a consequence of our measurement technique: since we use the same range of powers for the tomography experiment at each current, we achieve lower count rates and hence higher errors when p_1 is lower. However, in an application where an unknown source has to be characterized, the intensity of that source typically cannot be increased by the experimenter, and at any given intensity the count rate at low bias currents will be lower. We therefore conclude that these error estimates describe a reasonable scenario.

We note that we have improved on the result presented in [88] by more than an order of magnitude. Two orders of magnitude (i.e. an accuracy of a few Angstrom) could easily be reached by decreasing the width of the wire, which makes the energy-current relation more steep, thereby improving energy resolution at a given bias current resolution.

In the inset of Figure 4.12, we plot the extrapolated accuracy with which we can determine a central wavelength as a function of that wavelength.

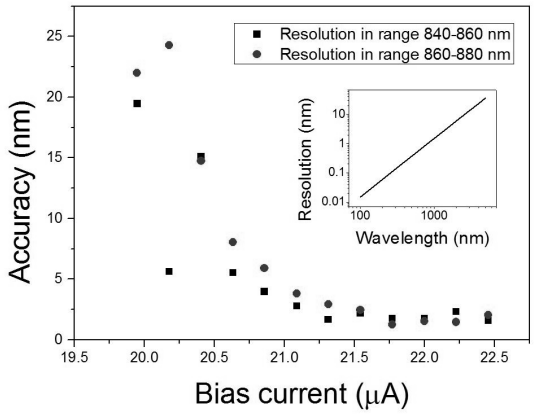

Figure 4.12: Observed wavelength accuracy as a function of bias current. We find that for higher bias currents the accuracy becomes better. The high-accuracy plateau between 21.5 and 22.5 μA corresponds to a accuracy of 1.4 nm. *Inset:* Extrapolated wavelength accuracy.

Since we expect our energy resolution to be constant, we obtain a wavelength resolution proportional to $1/\lambda^2$. We expect this wavelength resolution to break down at the point where the excitation becomes energetic enough for the normal state to start playing a role in the detection mechanism, which is predicted to happen at a photon energy in the UV [28]. In this energy range, the linear dependence will give way to a sub-linear dependence, reducing the resolution.

Lastly, we note one additional effect which becomes visible when zoomed in to this particular wavelength range: there is a step in the energy-current relation between 840 and 800 nm. While more work is clearly needed to explain this effect, it is intruiging that the first point which breaks the trend occurs at 820 nm. We note that our 820 $\pm$ 5 nm light coincides with the bandgap of GaAs at low temperatures, which is at 816 nm. We speculate that this effect is related to the absorption of light in our substrate, but note that this effect cannot be explained by invoking only the heating of the sample due to the increased absorption: as noted in the main text, this would decrease the amount of current required for a detection event rather than increase it. Noting that perhaps this effect is responsible for some of the spread between wavelengths $\Delta I = 250$ μA in Figure 4.2, we pass over this point without further interpretation.

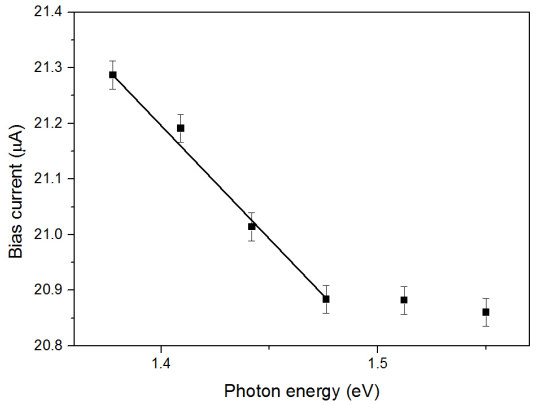

Figure 4.13: Experimental observation of a step in the energy-current relation, around 820 nm. We speculate that this effect is due to crossing the bandgap of GaAs at 816 nm.